

Softened sp^2 - sp^3 bonding network leads to strong anharmonicity and weak hydrodynamics in graphene+

Linfeng Yu¹, Ailing Chen¹, Xiaoxia Wang², Huimin Wang², Zhenzhen Qin³, and Guangzhao Qin^{1,*}

¹State Key Laboratory of Advanced Design and Manufacturing for Vehicle Body, College of Mechanical and Vehicle Engineering, Hunan University, Changsha 410082, P. R. China

²Hunan Key Laboratory for Micro-Nano Energy Materials & Device and School of Physics and Optoelectronics, Xiangtan University, Xiangtan 411105, Hunan, China

³School of Physics and Microelectronics, Zhengzhou University, Zhengzhou 450001, China

Abstract:

Graphene+, a novel carbon monolayer with sp^2 - sp^3 hybridization, is recently reported to exhibit unprecedented *out-of-plane* half-auxetic behavior and graphene-like Dirac properties [Yu *et al*, Cell Reports Physical Science, 3 100790 (2022)]. Herein, from comprehensively *state-of-the-art* first-principles studies, we reveal the effect of softened sp^2 - sp^3 bonding on the lattice thermal transport properties in graphene+. At room temperature, the thermal conductivity (κ) of graphene+ is ~ 170 W/mK, which is much lower than that of graphene (~ 3170 W/mK). It is found that the softened sp^2 - sp^3 bonding significantly suppresses the vibrations of acoustic phonons, which leads to strong anharmonicity and weak phonon hydrodynamics. Thus, the reduction in κ magnitude stems from the softened sp^2 - sp^3 bonding network. Our study provides fundamental physical insights into the thermal transport properties of graphene+, which would provide prospective guidance for its promising application in the field of thermal management.

Keywords: graphene+, sp^2 - sp^3 bonding, phonon hydrodynamics, strong anharmonicity.

1. Introduction

* Author to whom all correspondence should be addressed. E-Mail: gzqin@hnu.edu.cn

Recent decades have witnessed the vigorous development of carbon materials, and lots of excellent carbon materials have been reported, including diamond¹, T-carbon², and others^{3–5}. In particular, the successful fabrication of graphene opened the door to the world of two-dimensional (2D) materials⁶, which show excellent properties. Typically, graphene is widely used as a research benchmark in monolayer carbon materials due to its outstanding properties, such as electronic Dirac properties⁷, high breaking strength⁸, and ultra-high thermal conductivity (κ)⁹. In addition, the anisotropic negative Poisson's ratio (NPR) behavior can be induced mechanically in graphene^{10–13}. Furthermore, extensive efforts have been devoted to searching for promising 2D carbon candidates beyond graphene. For instance, Zhang *et al* found that pure pentagonal rings can form a novel 2D carbon allotrope, namely penta-graphene¹⁴, which serves as an excellent design platform for 2D penta-materials^{15–18}. Moreover, a series of 2D carbons with outstanding properties have been reported, such as T-graphene¹⁹, Twin-graphene²⁰, SW-graphene²¹, and biphenylene^{22,23}. Abundant configurations enable carbon materials to form a promising candidate library for micro-nano electronic devices. While in practical applications, the understanding of thermal transport is of great significance to the working lifetime and performance of micro-nano electronic devices, which demands fundamental study. However, despite the boom in carbon materials, insights into thermal transport properties remain challenging because of expensive experimental equipment and computational resources.

With the rich and diverse bonding configurations in carbon materials, the in-depth understanding of thermal transport properties in 2D carbon materials is becoming a central issue. For 2D carbon materials, the strong planar sp^2 hybrid C-C bond properties in graphene lead to its ultra-high κ of 3000–5000 W/mK^{9,24,25}. And Choudhry *et al.* reported that the reduced κ of graphene allotropes is due to phonon branches folding induced by the phononic crystal, independent of bond strength²⁶. In addition, T-graphene, D-graphene, and biphenylene have been reported to exhibit distinctive thermal transport behaviors due to diverse sp^2 bonding arrangement, with κ being 800, 600, and 166 (254) W/mK, respectively^{22,26}. However, the sp^3 hybridization effect is not considered in these studies. It has been reported that the sp^3 hybridization induces a strongly buckling structure in penta-graphene, which contributes to the large scattering phase space and low κ (645 W/mK) due to the broken *out-of-plane* symmetry²⁷. Such phenomenon also generally occurs in other 2D buckling compounds, such as

silicene²⁵, g-B₃N₅²⁸, and others^{29,30}. Interestingly, it is not found in our study, despite the similar buckling structures and pentagonal rings. Those diverse thermal transport behaviors largely originate from the different C-C bond morphology. Except penta-graphene with the sp^2 - sp^3 hybridization, previously reported studies involving thermal transport properties have mainly focused on carbon monolayers with sp^2 hybridization bonding networks. It remains poor knowledge of how the complex sp^2 - sp^3 (or sp^3) hybrid bonding affects the thermal transport properties.

Recently, a sp^2 - sp^3 hybrid carbon monolayer grapheneplus (graphene+) has been reported to possess an unprecedented novel *out-of-plane* half-auxetic behavior in our study³¹. The novel auxetic behavior caused by the sp^3 hybridization-induced geometric mode switching beyond graphene is expected to bring more interesting applications and prospects for graphene+. In addition, graphene+ also exhibits outstanding electronic Dirac properties. The excellent mechanical and electrical performance promise graphene+ to be a strong candidate for applications in electronics and thermal management. However, the unknown thermal transport properties and the fundamental understanding of the mechanism limit its further development. And the hybrid sp^2 - sp^3 bonding in graphene+ is expected to shed light on the fundamental understanding of the bonding effect on thermal transport.

In this paper, based on *state-of-the-art* first-principles calculations, we comprehensively explored the thermal transport properties of graphene+ with graphene as a benchmark comparison. One order of magnitude lower κ than graphene and exceptional thermal transport properties is found in graphene+. To reveal the origin, we conduct mode-level phonon property images and discuss the effects of lattice dynamics, four-phonon scattering, size effects and phonon hydrodynamics, which highlight the key role of quantified sp^2 - sp^3 bonding in thermal transport. The mechanism as revealed in this study is expected to provide an answer to the open question of how the atom bonding affects thermal transport, which would promote the applications of graphene+ and other carbon materials in electronics with high performance thermal management.

2. Computational Methodology

All first-principles calculations are performed with the aid of the Vienna *ab initio* simulation package (VASP)^{32,33} based on density functional theory (DFT). The Perdew–Burke–Ernzerhof (PBE)³⁴ is used to describe the exchange and correlation interactions between electrons. The kinetic energy cutoff of 1000 eV, 2.5 times the recommended value for carbon in the potential file, is selected to expand the wave functions in plane-wave basis set. A Monkhorst-Pack³⁵ \mathbf{q} -mesh of $9 \times 9 \times 1$ ($15 \times 15 \times 1$) is used to optimize the crystal structure for graphene+ (graphene) with the accuracy of 10^{-6} and 10^{-5} eV for energy and Hellmann-Feynman force convergence, respectively. The $2 \times 2 \times 1$ ($5 \times 5 \times 1$) supercell with $2 \times 2 \times 1$ \mathbf{q} -mesh is used to calculate second-order and third-order force constants for graphene+ (graphene). Based on harmonic and anharmonic force constants, the κ is obtained with the ShengBTE³⁶ code:

$$\kappa = \kappa_{\alpha\alpha} = \frac{1}{V} \sum_{\lambda} C_{\lambda} v_{\lambda\alpha}^2 \tau_{\lambda\alpha} , \quad (1)$$

where $\tau_{\lambda\alpha}$, C_{λ} , and $v_{\lambda\alpha}$, and V are relaxation time, specific heat capacity, group velocity for λ mode phonon along α direction, and crystal volume, respectively.

3. Results

3.1 Crystal structure and interatomic interactions

The top and side views of the crystal geometry for graphene and graphene+ are comparably shown in Fig. 1(a-d). As a typical sp^2 hybrid carbon monolayer, each carbon atom in graphene forms strong C-C bonds with three other carbon atoms. The difference between graphene+ and graphene is that the five-membered rings in graphene+ are distributed along the diagonal of the square to form a carbon network with sp^2 - sp^3 hybridization. The two sp^3 carbon atoms are in the center of the diagonal line, and the sp^2 carbon atoms form a plus "+" shaped distribution around the sp^3 carbon atoms, which is why it is called graphenepius (graphene+). Since the bonding in graphene+ deviates from the ideal sp^2 hybridization in graphene, *out of plane* half-auxetic behavior emerges in graphene+ despite exhibiting Dirac properties³¹. In particular, the thermal transport properties of graphene+ are also expected to

exhibit distinct extraordinary properties as a complement and candidate beyond graphene in the field of thermal management.

To evaluate the bonding strength and interaction range in graphene+, the normalized force constant trace (FCT) is calculated. Based on the finite displacement difference method in real space, interatomic force constant can obtain as the second derivative of the energy E by:^{37,38}

$$\frac{\partial^2 E}{\partial R_i \partial R_j} = \begin{bmatrix} \frac{\partial^2 E}{\partial R_x \partial R_x} & \frac{\partial^2 E}{\partial R_x \partial R_y} & \frac{\partial^2 E}{\partial R_x \partial R_z} \\ \frac{\partial^2 E}{\partial R_y \partial R_x} & \frac{\partial^2 E}{\partial R_y \partial R_y} & \frac{\partial^2 E}{\partial R_y \partial R_z} \\ \frac{\partial^2 E}{\partial R_z \partial R_x} & \frac{\partial^2 E}{\partial R_z \partial R_y} & \frac{\partial^2 E}{\partial R_z \partial R_z} \end{bmatrix}, \quad (2)$$

where R_α represents the position of the atom along the α direction. The normalized FCT are calculated to assess the relative strength of the bonding between different atoms with different spacing^{37,38}, thereby further determine their interaction range:³⁷

$$\text{FCT} = \frac{\partial^2 E}{\partial R_x \partial R_x} + \frac{\partial^2 E}{\partial R_y \partial R_y} + \frac{\partial^2 E}{\partial R_z \partial R_z}, \quad (3)$$

$$\text{normalized FCT} = \frac{\frac{\partial^2 E}{\partial R_{0,x} \partial R_{n,x}} + \frac{\partial^2 E}{\partial R_{0,y} \partial R_{n,y}} + \frac{\partial^2 E}{\partial R_{0,z} \partial R_{n,z}}}{\frac{\partial^2 E}{\partial R_{0,x} \partial R_{0,x}} + \frac{\partial^2 E}{\partial R_{0,y} \partial R_{0,y}} + \frac{\partial^2 E}{\partial R_{0,z} \partial R_{0,z}}}, \quad (4)$$

where $\frac{\partial^2 E}{\partial R_{i,x} \partial R_{j,\alpha}}$ denotes the harmonic force constant of the interaction between the i^{th} atom and the j^{th} atom along the x direction. When $i=j=0$, $\frac{\partial^2 E}{\partial R_{i,x} \partial R_{j,\alpha}}$ represents the self-interaction force constant along the α direction. Correspondingly, when $i=0, j=n$, it represents the force constant of the atom of the n^{th} nearest neighbor relative to the initial (labeled "0") atom. The cutoff radius (r^{cutoff})-dependent normalized FCT behavior enables the evaluation of long-range interactions between atoms, which successfully explained the long-range effect of the resonant bonding in the rock-salt structures such as bulk PbX (X=S, Se, and Te) and monolayer black phosphorene^{37,39-42}.

According to Eq. (2-4), the result of the normalized FCT for graphene+ is plotted in Fig. 1(e). When the r^{cutoff} exceeds 2.5 Å, the normalized FCT values display obvious convergence. As the r^{cutoff} increases, the normalized FCT do not change significantly, especially when $r^{\text{cutoff}} > 4$ Å. Such behavior implies weak long-range interactions in graphene+. The reason may lie in that the introduction of sp^3 hybridization in graphene+ destroys the original ring-shaped large π bond to form a brand-new bonding morphology, while the π bond induces a long-range resonance in graphene³⁵. In addition, the r^{cutoff} -dependent κ behavior also suggests weak long-range interactions as shown in the inset of Fig. 1(e). The slight error in the κ oscillations may result from the initial random guess of the charge density in DFT calculations. Therefore, 5.4 Å is selected as the effective r^{cutoff} to obtain a satisfactory and strictly convergent κ , which includes the weak long-range interactions and the possible anharmonic effects.

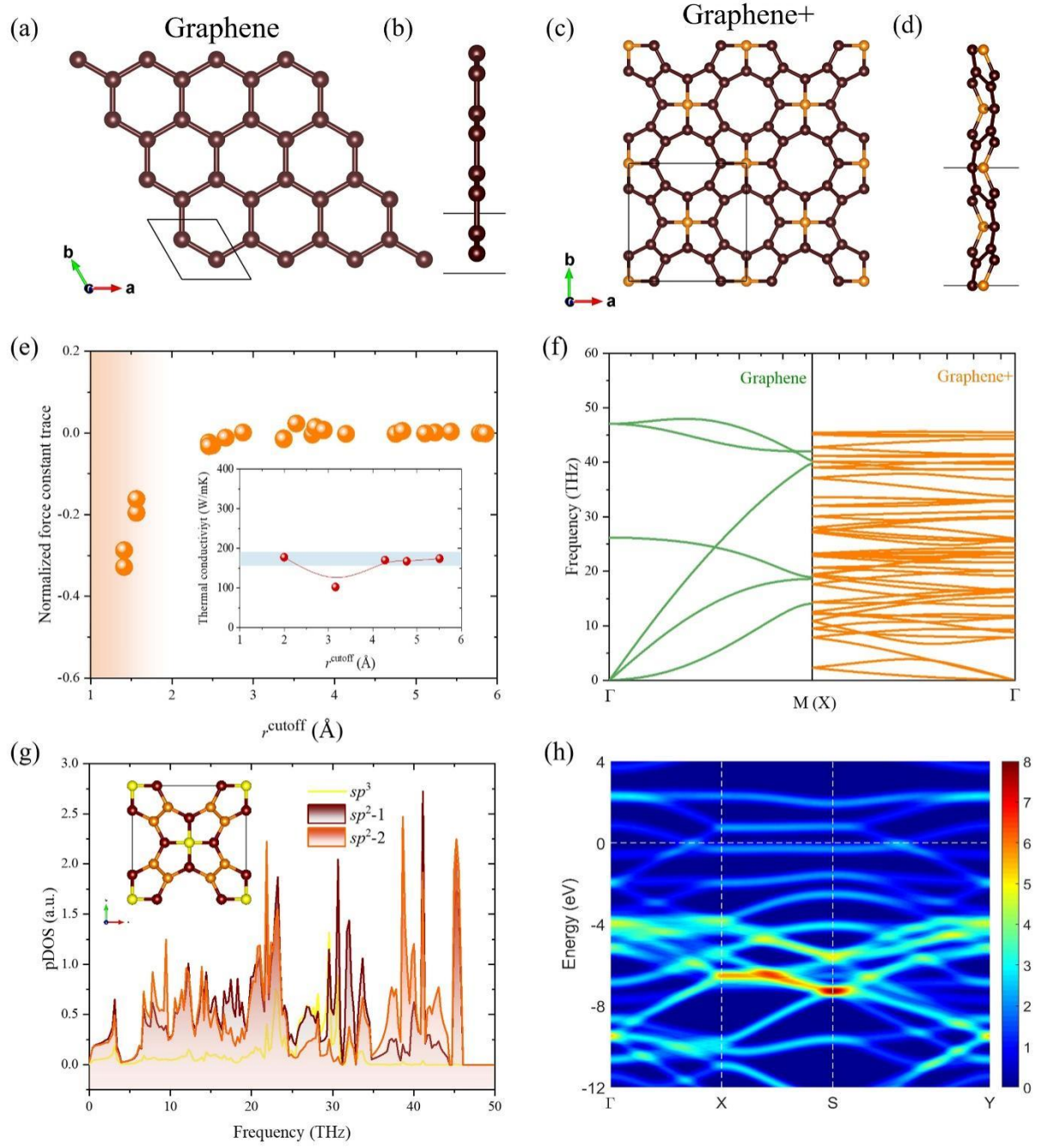


Figure 1. (a) Top and (b) side views for Graphene. (c) Top and (d) side views for Graphene+. (e) Normalized force constant trace and the insert is that thermal conductivity at 300 K as a function of cutoff radius (r^{cutoff} in Å) for graphene+. The light blue shading marks a 10% error area relative to the κ at $r^{\text{cutoff}} = 5.4$ Å. (f) The comparison of phonon dispersion for graphene and graphene+. (g) The

partial density of states ($pDOS$) of graphene+. The inset marks the atoms in sp^3 and sp^2 hybridization with different colors. (h) Inhomogeneous electron distribution in the energy bands of graphene+.

3.2 Competitive mechanism of lattice dynamics

The lattice dynamics and related thermal transport properties for graphene and graphene+ can be evaluated based on the phonon dispersion, which are plotted in Fig. 1(f). Almost the same phonon vibrational frequency range (0-50 THz) is manifested in the phonon dispersion for graphene and graphene+. However, due to the unique sp^2 - sp^3 network, more complex phonon dispersion appears in graphene+, arising a competing mechanism, namely the phonon beam and softened phonons. The concentrated phonon bands appear flatter in the phonon dispersion of graphene+, leading to the phonon beam effect⁴³. With the phonon beam effect, the small gap between the phonon bands makes it difficult for three phonons with close frequencies to be scattered, whether absorbed or emitted²⁹. As a result, it can effectively reduce the phonon scattering phase space [Fig. 3(c)] and improve κ . Simultaneously, the three acoustic phonon branches at low frequencies are depressed below 10 THz due to the substantial filling of the phonon band. The maximum phonon frequencies (ω_A) of the acoustic phonon branch at the high symmetry point M or X are 39.8 and 7.9 THz for graphene+ and graphene, respectively. Based on the equation of $\theta_D = \hbar\omega_A/k_B$ (\hbar , k_B are Planck constant and Boltzmann constant, respectively), lower Debye temperature θ_D is obtained in graphene+ (378 K) compared to graphene (1910 K). It is well-known that frequency-reduced acoustic phonon modes are more easily scattered in thermal vibrations due to lower Debye temperature. Therefore, the competing mechanism of phonon beam and softened phonons in graphene+ is expected to bring exceptional thermal transport behaviour, demanding for comprehensive investigations.

Softened phonon modes (weak lattice vibrations) indicate weakened sp^2 - sp^3 bonding, which can be reflected in mechanical properties. The Young's modulus (E) describes the physical quantity of a solid material's ability to resist deformation, and its decrease laterally exhibits softening of the bond. The E of graphene+ is calculated to be 120 N/m, which is much lower than that of graphene (320-350 N/m)³¹. Moreover, the contribution of sp^2 and sp^3 carbon atoms to the lattice vibrations is revealed by

the phonon partial density of states ($pDOS$) [Fig. 1(g)]. It is shown that the vibrations of sp^2 atoms cover the entire frequency range, while the sp^3 carbon atoms mainly contribute to the phonon vibrational frequency range of 20-35 THz. The reason may lie in that sp^3 hybridization has relatively weak bonding to soften the phonon mode. Moreover, direct insight can be gained into weak bonding from the distribution of electrons in the energy bands as shown in Fig. 1(h). Compared to pure sp^2 hybridization in graphene^{25,44}, the occupancy distribution of electrons in the graphene+ orbitals is more inhomogeneous and thus is likely to provide more anharmonicity.

3.3 Thermal conductivity

To further explore the effect of sp^2 - sp^3 bonding on thermal transport, the temperature-dependent κ behavior is obtained for graphene+, in comparison with graphene as shown in Fig. 2(a). The κ based on the iterative (ITE) method is ~ 170 and ~ 3170 W/mK for graphene+ and graphene, respectively. The κ of graphene calculated in this work agrees well with the previously reported results of 3000-5000 W/mK^{9,24,45}. The κ of graphene+ is one order of magnitude lower than that of graphene, and also lower than well-known high- κ materials such as diamond (~ 2000 W/mK)⁴⁶, c-BAs (~ 1000 W/mK)^{43,47-49} and TaN (~ 900 W/mK)^{50,51}, but still higher than MoS₂ (23.15 W/mK)⁵², silicene (~ 20 W/mK)^{30,53}, black phosphorene (~ 15 W/mK along zigzag direction and ~ 5 W/mK along armchair direction)³⁹, *etc.* The κ calculated by relaxation time approximation (RTA) method is 440 W/mK for graphene, which is almost one order of magnitude underestimated compared to the iterative (ITE) method, revealing the strong phonon hydrodynamic effect in graphene. In contrast, the RTA method evaluates the κ of graphene+ to be ~ 110 W/mK, which is 35% lower than the iterative κ , implying weak phonon hydrodynamics in graphene+ as discussed in Sec. 3.5.

The percentage contributions of different phonon branches to the total κ are shown in Fig. 2(b) and (c) for graphene+ and graphene, respectively. For graphene, the κ is mainly contributed by the FA branch phonons, which almost exceeds 50% in the temperature range of 200-800 K. Especially at room temperature, the percentage contribution of the FA branch exceeds 80%, which is consistent with previous studies^{25,44}. In addition, the contribution of TA to κ in graphene increases slightly with

temperature, but it is not enough to completely dominate the κ . As for the optical branch, it contributes little to the κ . Similar to graphene, the FA branch in graphene+ also occupies a slightly larger contribution compared to the other branches. At room temperature, The FA contribution exceeds 50% and is almost decisive for κ , but still weaker than that of graphene. Most differently, the contribution of the optical branch in graphene+ increases significantly with increasing temperature, which contributes almost as much as the FA branch ($\sim 40\%$) at 800 K. The enhancement of optical phonon branches would empower graphene+ efficiently dissipate heat at high temperatures^{54,55}.

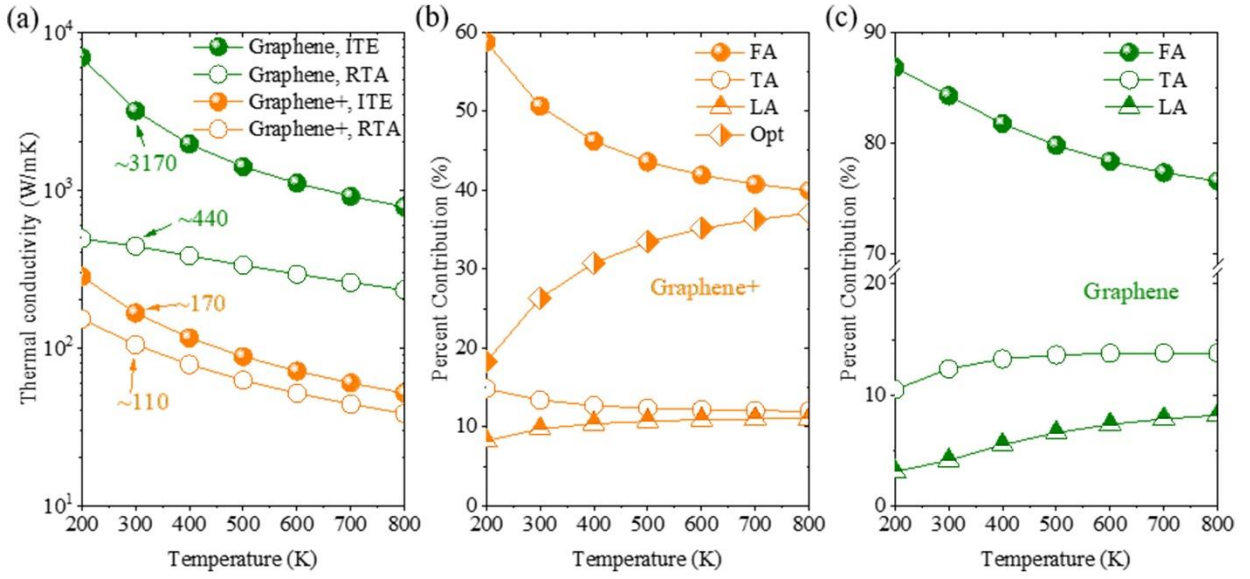


Figure 2. Thermal transport properties as a function of temperature. (a) Lattice thermal conductivity of graphene+ and graphene as a function of temperature. The percentage contribution of each phonon branch to thermal conductivity as a function of temperature for (b) graphene+ and (c) graphene. The FA, TA, and LA represent the flexible, transverse, and longitudinal acoustic phonon branches, respectively, and Opt represents the sum of the optical phonon branches.

3.4 Phonon properties

To reveal the origin of the large reduction in the κ of graphene+ compared to graphene, the phonon properties of different modes over the entire frequency vibrational range are comprehensively

investigated. The group velocity is derived from the derivation of the phonon dispersion with respect to the phonon wavenumber:

$$v = \frac{\partial \omega}{\partial q}, \quad (5)$$

The phonon relaxation time is derived from the reciprocal of scattering rate, *i.e.*, $\Gamma = \frac{1}{\tau}$. Based on Matthiessen's rule⁵⁶, summing different scattering events gives the total scattering rate as follows:

$$\frac{1}{\tau(\vec{q}, p)} = \frac{1}{\tau^{anh}(\vec{q}, p)} + \frac{1}{\tau^{iso}(\vec{q}, p)} + \frac{1}{\tau^B(\vec{q}, p)}, \quad (4)$$

where $1/\tau^{anh}$, $1/\tau^{iso}$, and $1/\tau^B$ are anharmonic (three-phonon), isotopic, and boundary scattering, respectively.

The results of mode-level phonon properties are plotted in Fig. 3. The group velocity measures the speed of phonons in thermal transport, where higher group velocity generally means higher κ . As shown in Fig. 3(a), the group velocity of graphene is much higher than that of graphene+. For instance, the highest group velocity of graphene+ is lower than 20 km/s while graphene is higher. In addition, the group velocity of phonons with frequencies of 0-10 THz in graphene increases rapidly and is generally higher than 5 km/s. However, such phenomenon is not observed in graphene+, which is caused by the strong softening of the FA branch in graphene+ as previously discussed in Fig. 1(f).

As shown in Fig. 3(b), the relaxation time of graphene is much higher than that of graphene+, which is almost one order of magnitude higher. In particular, the relaxation time of graphene+ tends to decrease sharply in the range of 0-7 THz, which makes the relaxation time of graphene+ nearly two orders of magnitude lower than that of graphene. Namely strong phonon-phonon scattering exists in the low frequency region for graphene+. To measure phonon-phonon scattering, the mode-level scattering phase space and the Grüneisen parameters are provided in Fig. 3(c) and (d), respectively. Commonly, buckling structures tend to result in large scattering phase spaces^{29,57}, allowing for high possibility of scattering between phonons. For instance, a low κ of ~20 W/mK is found in silicene due to the fact that the *out-of-plane* buckling structure breaks the symmetry^{57,58}. In addition, penta-graphene is also found to have a larger phase space, which contributes to the low κ ⁴⁵. In contrast, Fig.

3(c) reveals that graphene+ possesses a smaller scattering phase space compared with graphene. And its origin can be traced back to its unique phonon beam effect, as shown in the inset of Fig. 3(c). Since the phonon branches are close to each other, this suppresses the direct scattering between phonons on adjacent branches due to not satisfying energy conservation. Thus, the strong phonon-phonon scattering of graphene+ must originate from the large Grüneisen parameter representing strong anharmonicity considering the small scattering phase space. As shown in Fig. 3(d), and the inset in Fig. 3(e), larger mode-level and total Grüneisen parameters imply high scattering intensity, revealing strong anharmonicity. The strong anharmonicity is attributed to the softened phonon modes, which overcomes the small scattering phase space and leads to the large phonon scattering rate. Moreover, it can be intuitively revealed by the 3D electron localization function (ELF) as shown in the inset of Fig. 3(d), where the inhomogeneous electrons are localized around the carbon atoms in graphene+ while remains neatly distributed in graphene.

The differences in the phonon properties can be fundamentally analyzed from the mode-level κ as shown in Fig. 3(e). The cumulative κ of graphene and graphene+ increases rapidly with increasing frequency. When the phonon frequency lies in 0-10 THz, the κ of graphene increases the fastest, indicating phonons with frequencies of 0-10 THz dominate the lattice vibrations. Hence, the reduced κ of graphene+ lies in the softened low-frequency acoustic phonons, which is consistent with the contribution from phonon branches [Fig. 2]. Note that the dominant frequency range of the κ contribution is the same as the vibrational range of sp^2 atoms [Fig. 1(f)]. Therefore, the thermal transport is mainly governed by the phonons from the sp^2 carbon atomic vibrations in graphene+ while the existence of sp^3 carbon atoms will suppress the κ .

The discussion above treats three-phonon scattering as the dominant scattering process. However, four-phonon scattering may play an important role. Typically, the strong four-phonon scattering mainly originates from the phonon bands decoupled by the wide phonon band gap^{47-49,59}. For instance, the wide phonon band gap in c-BAs leads to a much larger phase space for four-phonon scattering ($P_4 = 3.9 \times 10^{-3}$) than three-phonon scattering ($P_3 = 3.8 \times 10^{-4}$). To evaluate the four-phonon effect in graphene+, the comparison of the P_4 and P_3 as a function of the $N \times N \times 1$ grid is provided in Fig. 3(f).

It is shown in graphene+ that the P_3 is significantly higher than P_4 , which means that three-phonon scattering dominates the phonon-phonon scattering process. In addition, the mode-level scattering phase space ratio P_4/P_3 is calculated to measure the effect of four-phonon scattering in graphene+ as shown in the insert of Fig. 3(f). The ratio P_4/P_3 below 1 exhibits a weak four-phonon process, especially at low frequencies, in sharp contrast to c-BAs ($P_4/P_3 \sim 10$). The weaker four-phonon effect in graphene+ is due to the narrow phonon band gap from the same atomic mass, while the wide band gap is induced by the large atomic mass difference between As and B atoms in c-BAs⁴³. Therefore, three-phonon scattering dominates thermal transport for all the phonons in graphene+, and the κ calculated based on three-phonon scattering is acceptable.

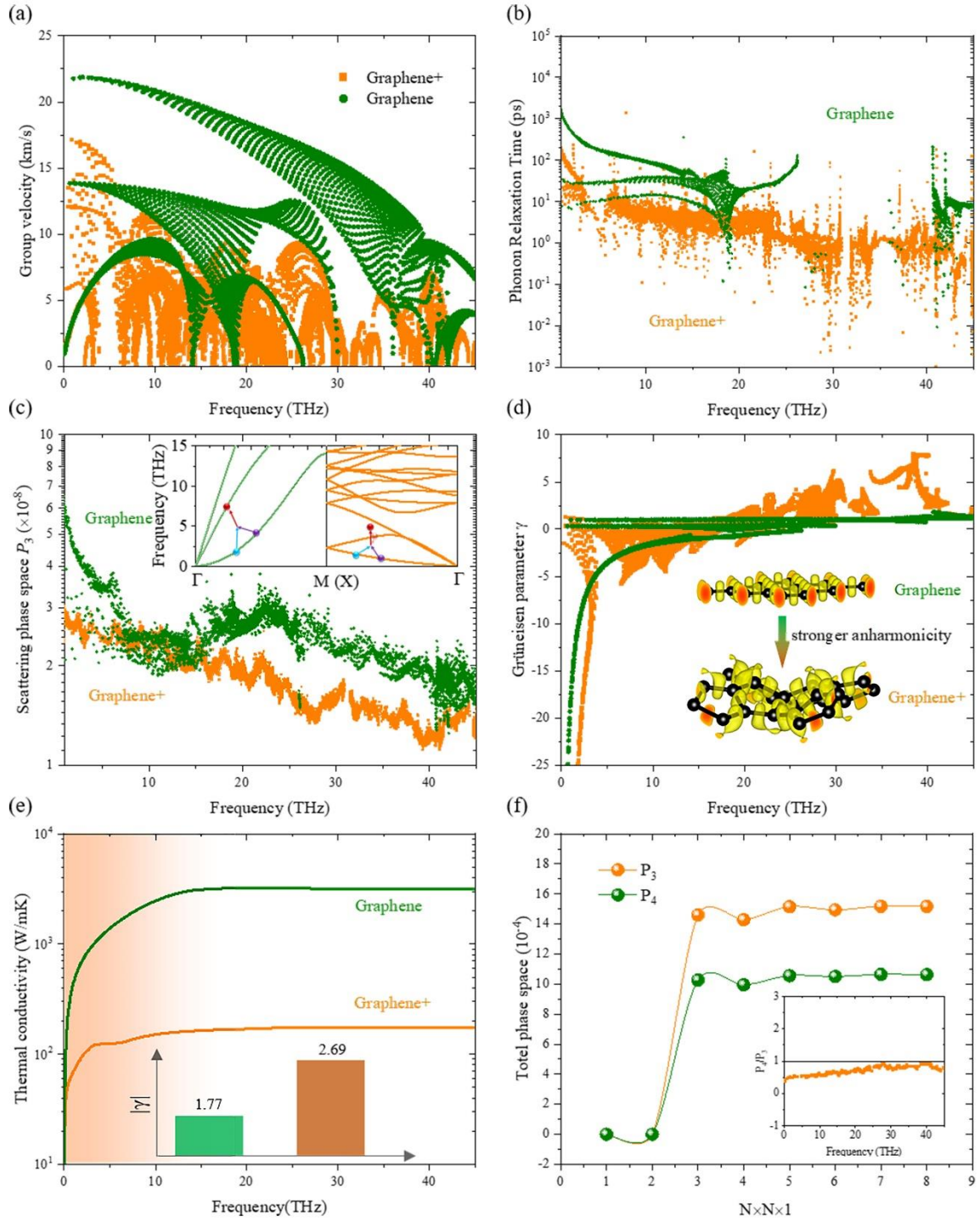


Figure 3. The mode-level (a) group velocity, (b) relaxation time, (c) scattering phase space, and (d) Grüneisen parameter at 300 K. (e) Cumulative thermal conductivity with frequency. (f) Comparison of the three- and four-phonon scattering phase spaces of graphene+. The insert is the frequency resolved ratio of the scattering phase space for three- to four-phonon processes for graphene+.

3.5 Phonon hydrodynamic effect

Phonon hydrodynamics^{60,61} in graphene are closely related to size effects, which can also be captured in transition metal chalcogenides⁶². Here, the cumulative κ as a function of mean free path (MFP) is plotted in Fig. 4(a). Based on the phonon gas model: $\kappa \sim \frac{1}{3}Cv l$, where C , v , l represent the specific heat capacity, group velocity and mean free path, respectively. Phonons with larger MFP tend to be less scattered, which contributes to higher κ . The MFP of graphene+ is in the range of 10 – 10^5 nm, nearly lower than graphene (10^2 – 10^5 nm). Further, the MFP corresponding to 50% of the cumulative κ is selected as the representative MFP (rMFP) to characterize the size effect on thermal transport. The rMFP of graphene is ~ 1150 nm, consistent with previous predictions²⁵. Due to its smaller group velocity and relaxation time, the rMFP of ~ 300 nm for graphene+ is an order of magnitude lower than graphene. This means that softened bonding results in lower rMFPs and narrower MFPs, which can reveal the movement patterns of phonons during transport as discussed below.

Phonon hydrodynamics means that phonons exhibit fluid-like macroscopic drift motions, namely the momentum-conserving collisions between a large number of phonons lead to the hydrodynamic flow during thermal transport. In such collisions, freezing reduces the wavelength of thermally excited phonons, thereby preserving momentum and becoming normal (N) scattering events. On the contrary, when the wave vector generated by scattering between two phonons exceeds the unit vector of the reciprocal lattice, the excess momentum is lost to the underlying lattice. Such phenomena are defined as umklapp (U) scattering events because they require sufficiently large wave vectors. The phonon hydrodynamics can be evaluated by the collision of the N and U process, and the three-phonon scattering process is determined by the conservation of momentum⁶³:

$$\vec{q} \pm \vec{q}' = \vec{q}'' + \vec{K}. \quad (7)$$

where $\vec{K} = 0$ and $\vec{K} \neq 0$ are N and U processes, respectively.

The quadratic FA branch in graphene leads to the large scattering phase space of normal (N) processes overtaking umklapp (U) processes, which contributes to the strong hydrodynamic effect⁵⁸. In graphene+, the softened sp^2 - sp^3 bond suppresses the acoustic phonon branches, making them flatter, which leads to a predictably weak hydrodynamic effect. The phonon-phonon scattering rates contributed by N and U are plotted in Fig. 4(b). In both graphene and graphene+, the U process contributes a stronger scattering rate than the N process, which means that the N process has a larger relaxation time and contributes more to κ while the U process contributes less. Note that the contribution of the N process to κ in graphene+ is weaker than that in graphene due to the strong N process scattering rate. The relative strength of N and U processes can be measured by their mode-level ratio (N/U) as the inserted in Fig. 4(c). Obviously, graphene+ (orange insert) exhibits a weaker phonon hydrodynamic effect compared to graphene (green insert), because the N/U value is greater than 1 in the 0-10THz region where phonons dominate the κ . Another intuitive evidence of hydrodynamics is the phonon Poiseuille flow, which can be quantified by the exponential power of κ as a function of temperature^{64,65}. By fitting the κ versus temperature relationship $\kappa \sim T^c$, $c = 1.3$ is obtained for graphene+ but $c = 1.8$ is for graphene. A low exponential factor means weak Poiseuille flow, *i.e.*, weak hydrodynamics. In graphene, long-range phonons ensure that phonon scattering is achieved in reciprocal space (N process). In contrary, the reduced MFP tends to make phonons more inclined to complete U process scattering across the Brillouin zone in graphene+. As shown in Fig. 4(a), the rMFP obtained by the ITE method in graphene (RTA: $\sim 74 \rightarrow$ ITE: ~ 1150 nm) is two orders of magnitude higher than the RTA method, while the rMFP of graphene+ is an order of magnitude growth (RTA: $\sim 91 \rightarrow$ ITE: ~ 300 nm), *i.e.*, The strong hydrodynamics lead to a significant improvement in rMFA for graphene: $\Delta \text{MFP}_{\text{gra}} = 14.5 > \Delta \text{MFP}_{\text{gra}+} = 2.3$, where $\Delta \text{MFP} = \frac{\text{rMFP}_{\text{ITE}} - \text{rMFP}_{\text{RTA}}}{\text{rMFP}_{\text{RTA}}}$. Because the RTA method treats N-process collisions as thermal resistance, RTA-based phonon-phonon scattering is severely overestimated in graphene as shown in Fig. 4(c), which leads to a significant underestimation of κ .

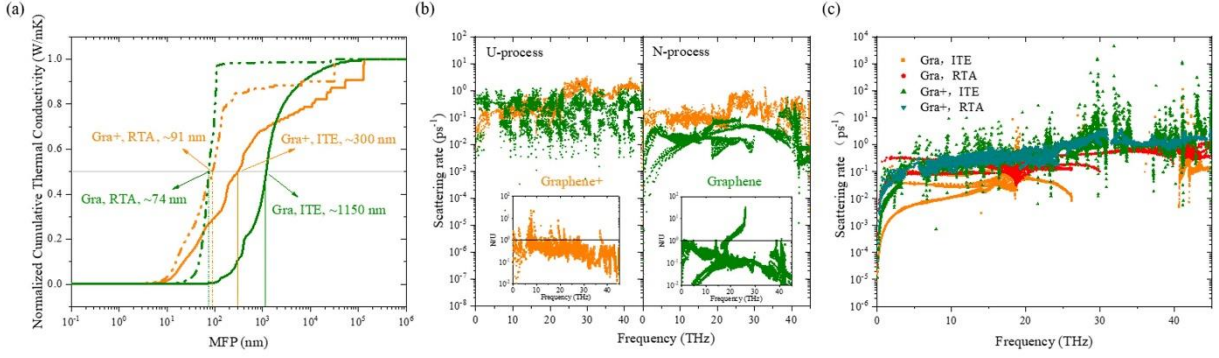


Figure 4. (a) Normalized thermal conductivity as a function of mean free path (MFP). (b) Comparative analysis of N and U processes in graphene+ and graphene. The insert is the ratio of the scattering rates of N to U processes. Orange and green represent graphene+ and graphene, respectively. (c) Comparison of phonon scattering rates based on iterative (ITE) and relaxation time approximation (RTA) methods for graphene+ (Gra+) and graphene (Gra).

To further demonstrate the weak hydrodynamics in the sp^2 - sp^3 network, the κ of several typical 2D carbon allotropes are evaluated based on ITE and RTA methods including penta-graphene (sp^2 - sp^3), biphenylene (sp^2), T-graphene (sp^2). The higher κ ratio $H=\kappa_{ITE}/\kappa_{RTA}$ of ITE to RTA means the stronger the hydrodynamics. As shown in Table 1, smaller H values are found in 2D sp^2 - sp^3 carbon allotropes compared with sp^2 hybridization, *i.e.*, $H_{gra+}=1.56 < H_{penta}=1.61 < H_{bip}=1.88$ or $2.03 < H_{T-gra}=2.65 < H_{gra}=7.20$, indicating that the introduction of sp^3 hybridization leads to a stronger negative effect on phonon hydrodynamics.

Table 1: Comparison of hydrodynamic effects in different hybridized two-dimensional carbon structures.

	κ_{ITE}	κ_{RTA}	$H=\kappa_{ITE}/\kappa_{RTA}$	Bond network
Graphene+	170	110	1.56	sp^2 - sp^3
Penta-graphene	437	272	1.61	sp^2 - sp^3
Biphenylene	267 (x)	142 (x)	1.88 (x)	sp^2
	421 (y)	207 (y)	2.03 (y)	
T-graphene	645	243	2.65	sp^2
Graphene	3170	440	7.20	sp^2

3.6 Quantification of interatomic bonding

Although the above analysis explains that weak bonding causes strong anharmonics and weak hydrodynamic effects, the weakening sp^2 - sp^3 network bonding is not well quantified. The restoring force of lattice atoms when vibrating near the equilibrium position can be evaluated by the potential well, which reflects the strength of the bonding between atoms^{25,66}. The potential well describes the relationship between the potential energy of the system and the positive and negative atomic displacement, and it can be obtained by applying positive and negative strain. As shown in Fig. 5(a), at the same potential level, the wider potential well of graphene+ means that it needs more energy to recover to the equilibrium position, which indicates the weak restoring force and atomic bonding.

The weak restoring force and bond strength can be further evaluated by the mean square displacement (MSD), which describes the amplitude of the lattice vibration at the equilibrium position and its sensitivity to the potential energy surface. MSD can be obtained by tracking the evolution of atomic positions in the system with time based on molecular dynamics, which is derived by:⁶⁷

$$\text{MSD}(m) = \frac{1}{N_{\text{particles}}} \sum_{i=1}^{N_{\text{particles}}} \frac{1}{N-m} \sum_{k=0}^{N-m-1} (\mathbf{r}_i(k+m) - \mathbf{r}_i(k))^2,$$

where $N_{\text{particles}}$, N , $\mathbf{r}_i(t)$ are the number of atoms in the system, the number of frames in the simulation, and the position of atom i at simulation time t . Considering the weak precision of the empirical potential, *ab initio* molecular dynamics (AIMD) is performed to obtain the MSDs of graphene+ and graphene as shown in Fig. 5(b). The MSD ratio ($\text{MSD}_{\text{gra}}/\text{MSD}_{\text{gra+}}$) of graphene (MSD_{gra}) and graphene+ ($\text{MSD}_{\text{gra+}}$) is also plotted to assess the relative magnitudes within the simulation domain. Near the equilibrium position, the energy of atomic vibrations originates from thermal fluctuations ($k_B T$), contributing a deviation. In the simulations, a larger MSD than graphene is found in graphene+, implying that it requires more energy to recover further deviations due to wider potential well curve.

Based on the above discussion, weaker bonding is identified in graphene+ compared to graphene. The bonding form in graphene+ is more complex, where both sp^2 and sp^3 hybrid carbon atoms exist, while only sp^2 hybrid carbon atoms exist in graphene. Hence, the final step is to determine the relative

strength of the bonds between the different hybrid atoms. As shown in Fig. 5(c), the bonding strength between different hybrid atoms in graphene+ is quantified by the integrated Crystal Orbital Hamilton Population (ICOHP)^{68,69}. Smaller ICOHP indicates larger bonding state occupation by orbital electrons, *i.e.* stronger interatomic bonding. For graphene, the ICOHP of pure sp^2 bonds is -10.4 eF. As for graphene+, it possesses three types of bonding, including sp^2-sp^3 , sp^2-1 , and sp^2-2 bonds. Notably, the ICOHP of sp^2-sp^3 (-7.8 eF) bond is significantly lower than sp^2 bond in graphene, while sp^2-1 (-10.2 eF) and sp^2-2 (-9.3 eF) bonds hardly change. Hence, the origin of κ an order of magnitude lower than graphene in graphene+ can be fundamentally explained by softened sp^2-sp^3 bonding. In graphene allotropes with the sp^2 hybridized form, the change in κ is independent of the bonding strength, but depends on the band folding induced by the unique phononic crystal structure²⁶. Such an explanation cannot satisfy graphene+ with the sp^3 hybridization. In graphene+, the sp^3 hybridization softens the bonds, leading to strong anharmonicity, especially those adjacent to sp^3 -hybridized carbon atoms (sp^2-sp^3 bond).

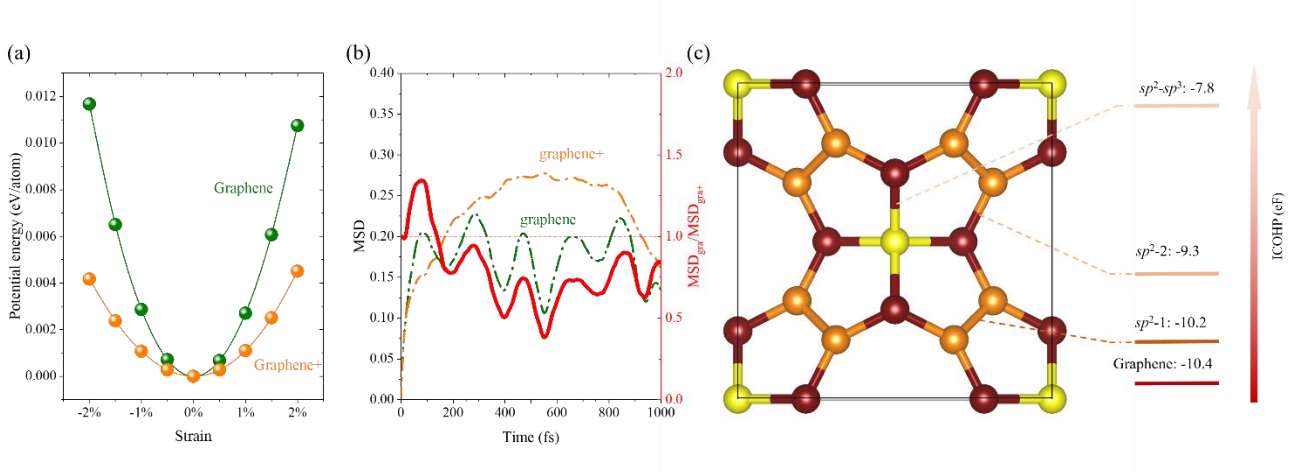


Figure 5. (a) Comparison of potential wells. (b) Root mean square displacement (MSD) based on ab initio analysis dynamics. (c) The integrated Crystal Orbital Hamilton Population (ICOHP) for different hybrid bonds.

4. Conclusion

In summary, we investigate the thermal transport properties of a novel 2D carbon monolayer graphene+ with sp^2 - sp^3 hybrid using *state-of-the-art* first-principles calculations. It is found that the κ of graphene+ is an order of magnitude lower than that of graphene. The origin of low κ can be chalked up to softened bonding in the unique sp^2 - sp^3 bonding network, which suppresses the low-frequency phonons (0-10 THz) that dominate κ . The softened phonon modes induce strong anharmonicity and weak phonon hydrodynamic effects. Based on the analysis of mode-level phonon properties, the strong anharmonicity in graphene+ can be attributed to the large Grüneisen parameter, which overcomes the weak scattering space and thus leads to the low relaxation time. It can be revealed intuitively through the inhomogeneous electron distribution in the band and electron localization function. Weak hydrodynamic effects are captured phonon collisions based on momentum conservation process (N and U process) and the exponential factor c of the phonon Poiseuille flow. Smaller phonon MFPs ensure weaker N process collisions, and smaller c value indicates weaker phonon Poiseuille flow. Hence, stronger phonon-phonon scattering is found in graphene+ due to weaker hydrodynamics. Finally, we quantify the strength of interatomic bonding based on potential wells and MSD, and identify the strength of sp^2 - sp^3 and sp^2 bonding by ICOHP. The sp^3 atoms would severely soften the adjacent sp^2 - sp^3 bonding, and contribute to the low κ .

Our work reveals the effect of the introduction of sp^3 hybridization on phonon thermal transport, which leads to softened sp^2 - sp^3 bonding while sp^2 bonding strength hardly changes in graphene allotropes. The softened sp^2 - sp^3 bonding leads to strong anharmonicity and weak hydrodynamic effects, ultimately reducing κ . The factors that can describe changes in thermal transport in our study are listed in Table 2 and a comprehensive analysis provides clear physical insights into the effect of hybridized sp^2 - sp^3 bonding in graphene+ on thermal transport behavior. Due to weak scattering phase space like graphene, graphene+ is expected to serve as an ideal model to study atomic bonding versus thermal transport properties. Combined with its unique mechanical auxetic and electronic Dirac properties, the in-depth understanding of the thermal transport behavior for graphene+ can provide effective guidance for electronic devices and related thermal management applications.

Table 2. Contributions of different parameters to thermal conductivity (κ), plus sign "+" indicates positive contribution to increase thermal conductivity, on the contrary minus sign "-" indicates negative contribution. Thermal conductivity (κ), acoustic phonon frequency (w_A), Debye temperature (θ), specific heat capacity (C), group velocity (v), relaxation time (τ), scattering phase space (P_3), Grüneisen parameter, ratio of N process to U process scattering rate (N/U), representative mean free path (rMFP), the growth ratio of MFP for iterative (ITE) to relaxation time approximation (RTA) methods (Δ MFP), potential well energy (E), the factor of Poiseuille flow (c), the ratio of κ for ITE to RTA methods (H), the mean square displacement (MSD), and the integrated Crystal Orbital Hamilton Population (ICOHP).

	graphene+	graphene
κ	-	+
w_A	-	+
θ_D	-	+
C	-	+
v	-	+
τ	-	+
P_3	+	-
γ	-	+
N/U	-	+
rMFP	-	+
Δ MFP	-	+
E	-	+
c	-	+
H	-	+
MSD	-	+
ICOHP	-	+

ACKNOWLEDGEMENTS

This work is supported by the National Natural Science Foundation of China (Grant No. 52006057), the Fundamental Research Funds for the Central Universities (Grant Nos. 531119200237 and 541109010001), and the State Key Laboratory of Advanced Design and Manufacturing for Vehicle

Body at Hunan University (Grant No. 52175013). The numerical calculations in this paper have been done on the supercomputing system of the National Supercomputing Center in Changsha, and the Hefei advanced computing center.

AUTHOR CONTRIBUTIONS

G.Q. supervised the project. L.Y. performed all the calculations and analysis. All the authors contributed to interpreting the results. The paper was written by L.Y. with contributions from all the authors.

DECLARATION OF INTERESTS

The authors declare no competing interests.

References

1. Ekimov, E. A. *et al.* Superconductivity in diamond. *Nature* **428**, 542–545 (2004).
2. Sheng, X.-L., Yan, Q.-B., Ye, F., Zheng, Q.-R. & Su, G. T-Carbon: A Novel Carbon Allotrope. *Phys. Rev. Lett.* **106**, 155703 (2011).
3. He, C. *et al.* Complex Low Energy Tetrahedral Polymorphs of Group IV Elements from First Principles. *Phys. Rev. Lett.* **121**, 175701 (2018).
4. Yang, X. *et al.* Novel Superhard s p³ Carbon Allotrope from Cold-Compressed C₇₀ Peapods. *Physical review letters* **118**, 245701 (2017).
5. Zhao, Z. *et al.* Novel superhard carbon: C-centered orthorhombic C₈. *Physical review letters* **107**, 215502 (2011).
6. Hashimoto, A., Suenaga, K., Gloter, A., Urita, K. & Iijima, S. Direct evidence for atomic defects in graphene layers. *Nature* **430**, 870–873 (2004).
7. Novoselov, K. S. *et al.* Two-dimensional gas of massless Dirac fermions in graphene. *Nature* **438**, 197–200 (2005).
8. Lee, C., Wei, X., Kysar, J. W. & Hone, J. Measurement of the Elastic Properties and Intrinsic Strength of Monolayer Graphene. *Science* **321**, 385–388 (2008).
9. Chen, S. *et al.* Thermal conductivity of isotopically modified graphene. *Nature Mater* **11**, 203–207 (2012).
10. Qin, Z., Qin, G. & Hu, M. Origin of anisotropic negative Poisson’s ratio in graphene. *Nanoscale* **10**, 10365–10370 (2018).

11. Qin, G. & Qin, Z. Negative Poisson's ratio in two-dimensional honeycomb structures. *npj Comput Mater* **6**, 51 (2020).
12. Jiang, J.-W. & Park, H. S. Negative Poisson's Ratio in Single-Layer Graphene Ribbons. *Nano Lett.* **16**, 2657–2662 (2016).
13. Jiang, J.-W., Chang, T., Guo, X. & Park, H. S. Intrinsic Negative Poisson's Ratio for Single-Layer Graphene. *Nano Lett.* **16**, 5286–5290 (2016).
14. Zhang, S. *et al.* Penta-graphene: A new carbon allotrope. *Proceedings of the National Academy of Sciences* **112**, 2372–2377 (2015).
15. Sun, S. *et al.* Flexible, auxetic and strain-tunable two dimensional penta-X₂C family as water splitting photocatalysts with high carrier mobility. *J. Mater. Chem. A* **7**, 7791–7799 (2019).
16. Liu, G., Zeng, Q., Zhu, P., Quhe, R. & Lu, P. Negative Poisson's ratio in monolayer PdSe₂. *Computational Materials Science* **160**, 309–314 (2019).
17. Lv, X. *et al.* Penta-MS₂ (M = Mn, Ni, Cu/Ag and Zn/Cd) monolayers with negative Poisson's ratios and tunable bandgaps as water-splitting photocatalysts. *J. Mater. Chem. A* **9**, 6993–7004 (2021).
18. Tao, W.-L., Zhao, Y.-Q., Zeng, Z.-Y., Chen, X.-R. & Geng, H.-Y. Anisotropic Thermoelectric Materials: Pentagonal PtM₂ (M = S, Se, Te). *ACS Appl. Mater. Interfaces* **13**, 8700–8709 (2021).
19. Liu, Y., Wang, G., Huang, Q., Guo, L. & Chen, X. Structural and Electronic Properties of $\sqrt{3}\sqrt{3}$ Graphene: A Two-Dimensional Carbon Allotrope with Tetrarings. *Phys. Rev. Lett.* **108**, 225505 (2012).
20. Jiang, J.-W. *et al.* Twin graphene: A novel two-dimensional semiconducting carbon allotrope. *Carbon* **118**, 370–375 (2017).
21. Yin, H. *et al.* Stone-Wales graphene: A two-dimensional carbon semimetal with magic stability. *Phys. Rev. B* **99**, 041405 (2019).
22. Veeravenkata, H. P. & Jain, A. Density functional theory driven phononic thermal conductivity prediction of biphenylene: A comparison with graphene. *Carbon* **183**, 893–898 (2021).
23. Fan, Q. *et al.* Biphenylene network: A nonbenzenoid carbon allotrope. *Science* **372**, 852–856 (2021).
24. Peng, B. *et al.* The conflicting role of buckled structure in phonon transport of 2D group-IV and group-V materials. *Nanoscale* **9**, 7397–7407 (2017).
25. Qin, Z., Qin, G., Zuo, X., Xiong, Z. & Hu, M. Orbital driven low thermal conductivity of monolayer gallium nitride (GaN) with planar honeycomb structure: a comparative study. *Nanoscale* **9**, 4295–4309 (2017).
26. Choudhry, U., Yue, S. & Liao, B. Origins of significant reduction of lattice thermal conductivity in graphene allotropes. *Phys. Rev. B* **100**, 165401 (2019).
27. Wang, F. Q., Yu, J., Wang, Q., Kawazoe, Y. & Jena, P. Lattice thermal conductivity of penta-graphene. *Carbon* **105**, 424–429 (2016).
28. Yu, L. *et al.* The synergistic modulation of electronic and geometry structures leads to ultra-low thermal conductivity of graphene-like borides (g-B₃X₅, X=N, P, As). *arXiv:2202.03622 [cond-mat]* (2022).
29. Yu, L. *et al.* Abnormal enhancement of thermal conductivity by planar structure: A comparative study of graphene-like materials. *International Journal of Thermal Sciences* **174**, 107438 (2022).
30. Peng, B. *et al.* Phonon transport properties of two-dimensional group-IV materials from *ab initio* calculations. *Phys. Rev. B* **94**, 245420 (2016).
31. Yu, L., Qin, Z., Wang, H., Zheng, X. & Qin, G. Half-negative Poisson's ratio in graphene⁺ with intrinsic Dirac nodal loop. *Cell Reports Physical Science* 100790 (2022) doi:10.1016/j.xcrp.2022.100790.

32. Kresse, G. & Furthmüller, J. “Efficient iterative schemes for ab initio total-energy calculations using a plane-wave basis set,” *Phys. Rev. B*, vol. 54, pp. 11169–11186. (1996).
33. Kresse, G. & Hafner, J. *Ab initio* molecular-dynamics simulation of the liquid-metal–amorphous-semiconductor transition in germanium. *Phys. Rev. B* **49**, 14251–14269 (1994).
34. Perdew, J. P., Burke, K. & Ernzerhof, M. Generalized Gradient Approximation Made Simple. *Phys. Rev. Lett.* **77**, 3865–3868 (1996).
35. Monkhorst, H. J. & Pack, J. D. Special points for Brillouin-zone integrations. *Phys. Rev. B* **13**, 5188–5192 (1976).
36. Li, W., Carrete, J., A. Katcho, N. & Mingo, N. ShengBTE: A solver of the Boltzmann transport equation for phonons. *Computer Physics Communications* **185**, 1747–1758 (2014).
37. Lee, S. *et al.* Resonant bonding leads to low lattice thermal conductivity. *Nat Commun* **5**, 3525 (2014).
38. Qin, G. & Hu, M. Accelerating evaluation of converged lattice thermal conductivity. *npj Comput Mater* **4**, 3 (2018).
39. Qin, G. *et al.* Resonant bonding driven giant phonon anharmonicity and low thermal conductivity of phosphorene. *Phys. Rev. B* **94**, 165445 (2016).
40. Wang, B.-T., Liu, P.-F., Zheng, J.-J., Yin, W. & Wang, F. First-principles study of superconductivity in the two- and three-dimensional forms of PbTiSe 2 : Suppressed charge density wave in 1 T – TiSe 2. *Phys. Rev. B* **98**, 014514 (2018).
41. Delaire, O. *et al.* Giant anharmonic phonon scattering in PbTe. *Nature Mater* **10**, 614–619 (2011).
42. Shportko, K. *et al.* Resonant bonding in crystalline phase-change materials. *Nature Mater* **7**, 653–658 (2008).
43. Lindsay, L., Broido, D. A. & Reinecke, T. L. First-Principles Determination of Ultrahigh Thermal Conductivity of Boron Arsenide: A Competitor for Diamond? *Phys. Rev. Lett.* **111**, 025901 (2013).
44. Wang, H. *et al.* Intrinsically low lattice thermal conductivity of monolayer hexagonal aluminum nitride (h-AlN) from first-principles: A comparative study with graphene. *International Journal of Thermal Sciences* **162**, 106772 (2021).
45. Wu, X. *et al.* Hydrogenation of Penta-Graphene Leads to Unexpected Large Improvement in Thermal Conductivity. *Nano Lett.* **16**, 3925–3935 (2016).
46. Slack, G. A. Thermal Conductivity of Pure and Impure Silicon, Silicon Carbide, and Diamond. *Journal of Applied Physics* **35**, 3460–3466 (1964).
47. Li, S. *et al.* High thermal conductivity in cubic boron arsenide crystals. *Science* **361**, 579–581 (2018).
48. Kang, J. S., Li, M., Wu, H., Nguyen, H. & Hu, Y. Experimental observation of high thermal conductivity in boron arsenide. *Science* **361**, 575–578 (2018).
49. Tian, F. *et al.* Unusual high thermal conductivity in boron arsenide bulk crystals. *Science* **361**, 582–585 (2018).
50. Kundu, A. *et al.* Ultrahigh Thermal Conductivity of θ -Phase Tantalum Nitride. *Phys. Rev. Lett.* **126**, 115901 (2021).
51. Guo, S.-D. & Liu, B.-G. Ultrahigh lattice thermal conductivity in topological semimetal TaN caused by a large acoustic-optical gap. *J. Phys.: Condens. Matter* **30**, 105701 (2018).
52. Guo, S.-D. Phonon transport in Janus monolayer MoSSe: a first-principles study. *Phys. Chem. Chem. Phys.* **20**, 7236–7242 (2018).
53. Taheri, A., Da Silva, C. & Amon, C. H. Phonon thermal transport in β - N X (X= P, As, Sb) monolayers: A first-principles study of the interplay between harmonic and anharmonic phonon properties. *Physical Review B* **99**, 235425 (2019).

54. Qin, G., Qin, Z., Wang, H. & Hu, M. Anomalously temperature-dependent thermal conductivity of monolayer GaN with large deviations from the traditional $1/T$ law. *Phys. Rev. B* **95**, 195416 (2017).
55. Wang, H., Qin, G., Li, G., Wang, Q. & Hu, M. Low thermal conductivity of monolayer ZnO and its anomalous temperature dependence. *Phys. Chem. Chem. Phys.* **19**, 12882–12889 (2017).
56. Qin, Z., Qin, G., Zuo, X., Xiong, Z. & Hu, M. Orbital driven low thermal conductivity of monolayer gallium nitride (GaN) with planar honeycomb structure: a comparative study. *Nanoscale* **9**, 4295–4309 (2017).
57. Gu, X. & Yang, R. First-principles prediction of phononic thermal conductivity of silicene: A comparison with graphene. *Journal of Applied Physics* **117**, 025102 (2015).
58. Xie, H., Hu, M. & Bao, H. Thermal conductivity of silicene from first-principles. *Appl. Phys. Lett.* **104**, 131906 (2014).
59. Feng, T., Lindsay, L. & Ruan, X. Four-phonon scattering significantly reduces intrinsic thermal conductivity of solids. *Phys. Rev. B* **96**, 161201 (2017).
60. Huberman, S. *et al.* Observation of second sound in graphite at temperatures above 100 K. *Science* **364**, 375–379 (2019).
61. Lee, S., Broido, D., Esfarjani, K. & Chen, G. Hydrodynamic phonon transport in suspended graphene. *Nat Commun* **6**, 6290 (2015).
62. Torres, P., Alvarez, F. X., Cartoixa, X. & Rurali, R. Thermal conductivity and phonon hydrodynamics in transition metal dichalcogenides from first-principles. *2D Mater.* **6**, 035002 (2019).
63. Wang, H. Intrinsically low lattice thermal conductivity of monolayer hexagonal aluminum nitride (h-AlN) from first-principles: A comparative study with graphene. *International Journal of Thermal Sciences* **8** (2021).
64. Gurzhi, R. N. THERMAL CONDUCTIVITY OF DIELECTRICS AND FERRODIELECTRICS AT LOW TEMPERATURES. **4**.
65. Guyer, R. A. & Krumhansl, J. A. Thermal Conductivity, Second Sound, and Phonon Hydrodynamic Phenomena in Nonmetallic Crystals. *Phys. Rev.* **148**, 778–788 (1966).
66. Lou, A., Liu, Q.-B. & Fu, H.-H. Enhanced thermoelectric performance by lone-pair electrons and bond anharmonicity in the two-dimensional Ge₂Y₂ family of materials with Y = N, P, As, or Sb. *Phys. Rev. B* **105**, 075431 (2022).
67. Wang, V., Xu, N., Liu, J.-C., Tang, G. & Geng, W.-T. VASPKIT: A user-friendly interface facilitating high-throughput computing and analysis using VASP code. *Computer Physics Communications* 108033 (2021) doi:10.1016/j.cpc.2021.108033.
68. Dronskowski, R. & Bloechl, P. E. Crystal orbital Hamilton populations (COHP): energy-resolved visualization of chemical bonding in solids based on density-functional calculations. *J. Phys. Chem.* **97**, 8617–8624 (1993).
69. Deringer, V. L., Tchougréeff, A. L. & Dronskowski, R. Crystal Orbital Hamilton Population (COHP) Analysis As Projected from Plane-Wave Basis Sets. *J. Phys. Chem. A* **115**, 5461–5466 (2011).